ACS OMEGA

http://pubs.acs.org/journal/acsodf

Article

Intrinsic Defects in $LiMn_2O_4$: First-Principles Calculations

Xu Li, Jianchuan Wang,* Shiwei Zhang, Lixian Sun, Weibin Zhang, Feng Dang, Hans J. Seifert, and Yong Du

Cite This: *ACS Omega* 2021, 6, 21255−21264

Read Online

ACCESS | Metrics & More | Article Recommendations | Supporting Information

ABSTRACT: Spinel $LiMn_2O_4$ has attracted wide attention due to its advantages of a high-voltage plateau, good capacity, environmental friendliness, and low cost. Due to different experimental synthesis methods and conditions, there are many intrinsic point defects in $LiMn_2O_4$. By means of first-principles calculations based on a reasonable magnetic configuration, we studied the formation energies, local structures, and charge compensation mechanism of intrinsic point defects in $LiMn_2O_4$. The formation energies of defects under the assumed O-rich equilibrium conditions were examined. It was found that O, Li, and Mn vacancies, Mn and Li antisites, and Li interstitial could appear in the lattice at some equilibrium conditions, but Mn interstitial is hard to form. The charge was compensated mainly by adjusting the oxidation state of Mn around the defect, except for the defects at the 8*a* Wyckoff site. The binding energies between point defects were calculated to shed light on the clustering of point defects. Furthermore, the diffusion of Li ions around the defects was discussed. Cation antisites led to a decrease of the Li diffusion barrier but O vacancy caused an increase of the barrier. This study provides theoretical support for understanding point defects in spinel $LiMn_2O_4$.

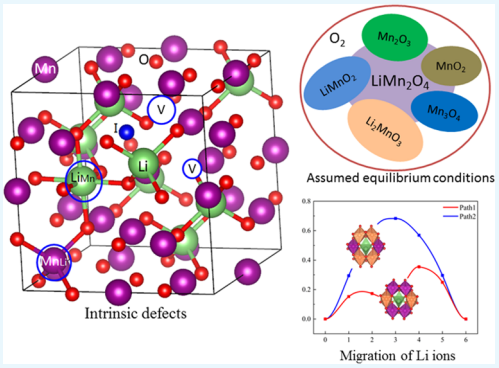

1. INTRODUCTION

Spinel $LiMn_2O_4$ is a typical manganese-based cathode material.[1−3] Thackeray et al. first proposed it as a cathode material for lithium-ion batteries.[4] In terms of battery performance, spinel $LiMn_2O_4$ has a high-voltage plateau (>4 V), good theoretical capacity density (148 mAh/g), and great thermal safety. More importantly, Mn has obvious advantages of low cost and nontoxicity. Consequently, $LiMn_2O_4$ is considered to be a substitute for layered $LiCoO_2$ on the electrodes of lithium-ion batteries.[5−8]

The cubic spinel structure of $LiMn_2O_4$ belongs to the $Fd\bar{3}m$ space group. Oxygen atoms, which are at 32*e* sites, are arranged in a cubic close-packed arrangement, lithium ions are located at 8*a* tetrahedral sites, and manganese ions occupy half of the octahedral positions, which are 16*d* sites. The other half of the octahedral void is 16c sites, which reside halfway between neighboring tetrahedral sites and serve as a channel for the migration of Li.[9−11] The average oxidation state of Mn in $LiMn_2O_4$ is +3.5, which is caused by a mixture of Mn^{3+} and Mn^{4+} in equal proportion, and its charge−discharge activity is the contribution of Mn^{3+}/Mn^{4+} redox.[12,13] The existence of the orbital-degeneracy Mn^{3+} ions will cause the Jahn−Teller (JT) effect during charging and discharging,[14−16] leading to unique properties such as structural distortions and phase transitions. On this account, the spinel $LiMn_2O_4$ transforms into an orthogonal phase when the temperature drops below 280 K,[17,18] and its magnetic ground state is antiferromagnetic (AFM).[19−21]

It is difficult to obtain the exact stoichiometric $LiMn_2O_4$ because of various synthetic methods and the synthetic environment. There would be various types of intrinsic point defects within the material, such as vacancies, interstitials, and metal antisite defects. Using powder X-ray diffraction and thermogravimetry analysis (TGA), Tarascon et al. found that some Mn ions are located in the tetrahedral sites of the spinel and a significant number of oxygens are lost,[22] suggesting that Mn antisites and O vacancies appear in $LiMn_2O_4$. Paulsen et al. also found that a certain amount of metal ion antisite defects, i.e., the antisites of Li and Mn, exist in Li_2MnO_4 at a wide range of temperatures.[23] Oh's group first applied differential pulse polarography to analyze the dissolved Mn^{2+} ions, which are generated by the disproportionation reaction $2Mn^{3+} \rightarrow Mn^{4+} + Mn^{2+}$ in the electrolyte.[24] They found that Mn dissolution was the primary reason for the capacity loss. With the dissolution of Mn, Mn vacancies are present in the 16*d* octahedral sites.

Following the formation of defects in the lattice, the spatial geometric environment and chemical environment of the surrounding atoms will change. As a result, the structure and

Received: March 3, 2021
Accepted: August 4, 2021
Published: August 12, 2021

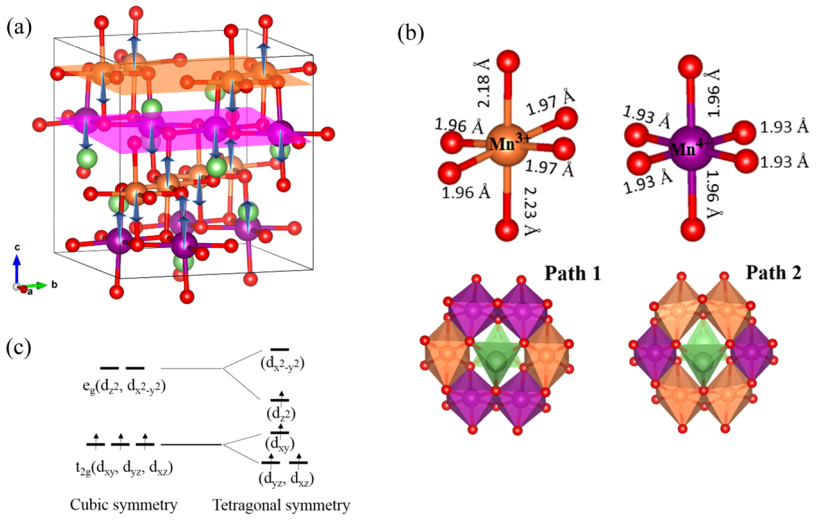

Figure 1. (a) Crystal and magnetic configurations of spinel-type $LiMn_2O_4$. Green spheres are Li, red spheres are O, yellow and purple spheres are Mn^{3+} and Mn^{4+}, respectively. The blue arrows indicate the direction of the magnetic moment of Mn. The Mn ions are with AFM configuration in the Mn^{3+} layer and with FM configuration in the Mn^{4+} layer. (b) The structure of Mn^{4+}-O_6 and Mn^{3+}-O_6 octahedrons and two paths for Li migration that consist of different oxidation states of Mn ions. (c) Schematic representation of electron distribution in the 3d orbital of Mn ions.

charge distribution of $LiMn_2O_4$ will change, which further affects the structure stability, charge voltage, and diffusion of ions in the material. Sugiyama et al. studied the effect of O vacancies (i.e., O deficiency) on the phase transition from cubic to the tetragonal phase of $LiMn_2O_4$ using differential scanning calorimetry (DSC), magnetic susceptibility, ^{7}Li nuclear magnetic resonance, and electronic resistivity.[25] Xia et al. studied the effects of Li defects and O vacancies on the structure and electrochemical properties of $LiMn_2O_4$.[26] They found that the capacity loss rate of anoxic materials is much faster, which is related to the phase transition in the cyclic process, in comparison with intact $LiMn_2O_4$. Besides experimental studies on defect-related properties in cathode materials, theoretic calculations, especially first-principles methods based on density functional theory (DFT), have been demonstrated to be a powerful tool for addressing defects in solid.[27,28] Some researchers have studied point defects in $LiMn_2O_4$ through computational methods.[20,21,29−32] As early as the 1990s, Islam's group have studied Li- and Mn-related interstitials and vacancies in $LiMn_2O_4$ using interatomic potential models.[32] Koyama et al. studied O vacancy, Li and Mn interstitials, Mn antisite, and some defect complexes in $LiMn_2O_4$ using the first-principles method.[29] They revealed that metal interstitials have lower formation energy compared with that of O vacancy. The excess Li are prone to occupy the 16*d* site other than the 16*c* site. Hoang has investigated cation point defects in $LiMn_2O_4$ in various possible charged states.[20] Recently, Xiao et al. studied the effect of Li-excess (it is in fact antisite Li in their work) on the diffusion of Li in $LiMn_2O_4$ using first-principles calculations and found that the Li-excess configuration enhances the Li ion diffusivity by introducing two new kinds of fast Li migration channels.[30]

As mentioned above, point defects are common in $LiMn_2O_4$ and may affect the electrochemical performance of $LiMn_2O_4$. Although there are some studies on point defects in $LiMn_2O_4$ by experimental or/and theoretic calculation methods in the literature, point defects are still not understood. For example, how is the distribution of point defects? What are the effects of defects on the charge distribution and charge compensation in the delithiation process? And how is the migration of Li when defects exist in the lattice? On the other hand, previous theoretic calculations have not carefully dealt with the magnetism of Mn in the lattice, except for the work of Xiao et al.[30] The spinel $LiMn_2O_4$ may have various magnetic configurations. Ouyang et al. considered the magnetic structures of $LiMn_2O_4$ with one ferromagnetic (FM) and two AFM arrangements of Mn ions. According to DFT calculations, they found that the AFM ordering of Mn chains along the [110] direction was more stable than other magnetic structures.[18] Recently, Liu et al. conducted extensive work on $LiMn_2O_4$ with different structures and magnetic configurations to find its ground state.[21] They used eight different AFM and two FM orders, including Ouyang's structures, and found that the most stable structure is a highly symmetrical configuration with alternating AFM (↑↓↑↓) layer and FM layer along the [001] direction. Koyama et al. and Huang just assumed a simple high-spin FM configuration of Mn to investigate point defects in $LiMn_2O_4$.[29,33] Different magnetic configurations will affect the ground-state structure of $LiMn_2O_4$ and further affect the properties of defects in the system. Therefore, to achieve accurate defect properties in $LiMn_2O_4$ computationally, it is better to investigate it based on a reasonable magnetic structure.

In this work, we use the first-principles calculation method based on DFT to comprehensively explore defect-related properties in spinel $LiMn_2O_4$. The formation energies of various isolated intrinsic point defects and the binding energies between point defects are calculated based on the lowest energy magnetic configuration proposed by Liu et al.[21] Furthermore, Bader charges are calculated to shed light on charge compensation associated with the creation of defects. Finally, we discuss the effect of defects on the diffusion of lithium ions. It is noteworthy that point defects in semiconductors and insulators may occur in charged states, and the thermodynamics of charged defects in $LiMn_2O_4$ have already been investigated by Hoang based on a ferromagnetic spin configuration.[20] Since the magnetic configuration used by Hoang is different from that of our work, we speculate that some conclusions on thermodynamics of charged point defects drawn from calculations based on the present magnetic

https://doi.org/10.1021/acsomega.1c01162
ACS Omega 2021, 6, 21255−21264

configuration may be inconsistent with the results of Hoang. Therefore, we will study charged defects in $LiMn_2O_4$ in future work, but only neutral defects are considered in the present work.

2. COMPUTATIONAL METHODOLOGY

DFT calculations were performed by the projector augmented wave (PAW) potential method, as implemented in the Vienna *ab initio* simulation package (VASP).[34] The interactions between electrons are treated by the generalized gradient approximation of Perdew and Wang with the Hubbard parameter correction (GGA+*U*).[35−38] The *U* values for the d-orbitals of Mn were set to 3.9 eV based on previous reports.[39,40] The electronic configurations of $1s^2 2s^1$, $3p^6 3d^5 4s^2$, and $2s^2 2p^4$ are employed as valence electrons for Li, Mn, and O, respectively, and all the other electrons are treated as core electrons. The conventional cubic spinel unit cell with the AFM magnetic configuration reported by Liu et al. was taken as the initial structure. The energy cutoff for the plane wave was set as 500 eV. The Brillouin zone was sampled by 2 × 2 × 2 special k-points using the Monkhorst−Pack scheme for geometry optimization, and 4 × 4 × 4 for the calculations of total energies and electronic structures. Geometry relaxation was complete when the residual forces acting on every atom were less than 0.02 eV $Å^{-1}$. Point defects were considered to have a low concentration in the bulk, so the cell volume and shape were fixed to the optimized crystal of bulk during the relaxation of defective lattice, and only atoms' coordinates were fully relaxed.

The climbing image nudged elastic band (CINEB) method was used to investigate the minimum energy pathways of ion hopping from one lattice site to the adjacent positions.[41,42] We insert five images during the CINEB calculation and the residual forces acting on every atom were less than 0.02 eV $Å^{-1}$. To describe the electron charge transfer between ions in the material, this paper adopts the Bader charge analysis method based on the charge density calculation.[43,44]

3. RESULTS AND DISCUSSION

3.1. Lattice and Magnetic Structure. The ground-state structure of $LiMn_2O_4$ is a highly symmetrical configuration with alternating AFM (↑↓↑↓) layer and FM layer along the [001] direction, as predicted by Liu et al.[21] Figure 1a shows the ground structure of $LiMn_2O_4$. After structural optimization, the cubic cell transforms into a tetragonally distorted cell with a lattice elongation of 7% along the *c* direction. The calculated lattice parameters ($a = b = 8.20$ Å and $c = 8.74$ Å) are consistent with the experimental data ($a = b = 8.11$ Å and $c = 8.65$ Å)[33] and previous calculated results ($a = b = 8.20$ Å and $c = 8.76$ Å; $a = b = 8.22$ Å and $c = 8.76$ Å).[21,30] The spinel $LiMn_2O_4$ is thus an orthorhombic lattice instead of a cubic one. Due to the magnetic structure, there are two different Mn−O_6 octahedral structures in the cell along the [001] direction. The specific octahedral structure and Mn−O bond length of the Mn−O_6 octahedrons are shown in Figure 1b. The purple Mn−O_6 octahedron is approximately a regular octahedron with the Mn−O bond length in the (001) plane being 1.93 Å and that in the *c* direction being 1.96 Å. However, the yellow Mn−O_6 octahedron has a large distortion. The four Mn−O bonds in the (001) plane are almost equal (1.96−1.97 Å), but the other two Mn−O bonds along the *c* direction (2.23 and 2.18 Å) are longer than these in the (001) plane. As mentioned previously, Mn^{3+} ions can cause JT distortion and thus the yellow Mn layer is rationally judged as the Mn^{3+} layer. The calculated Mn−O distances in the JT distorted MnO_6 octahedron agree well with the experimental data at 300 K (1.92 and 2.26 Å).[45] The conclusion is further supported by the atom's magnetic moments and Bader charges. The yellow Mn ion has a magnetic moment of 3.82 μ_B, while the purple Mn ion has about 3.13 μ_B. Note that the number of unpaired electrons of Mn^{4+} is less than that of Mn^{3+} (Figure 1c) and thus the yellow Mn is indeed in the + 3 state. Our calculated magnetic moments are consistent with the calculations by Liu et al.,[21] who reported the magnetic moments of Mn^{3+} and Mn^{4+} to be 3.9 μ_B and 3.2 μ_B, respectively. We further find that the Bader charge around Li is +0.89 e, and the Bader charges for yellow and purple Mn are +1.71 e and +1.84 e, respectively. For oxygen, due to different Mn ions around it, we denote O on the Mn^{3+} layer as $O_{Mn}{}^{3+}$. Similarly, the O on the Mn^{4+} layer is denoted as $O_{Mn}{}^{4+}$. We find that the Bader charges of the two O are almost equal (the Bader charges of $O_{Mn}{}^{3+}$ and $O_{Mn}{}^{4+}$ are −1.09 e and −1.13 e, respectively).

The JT effect originates from the orbital degeneration of transition metal ions. In spinel $LiMn_2O_4$, $Mn^{3+}(t_{2g}{}^3, e_g{}^1)$ is a JT ion, which will cause distortion of the surrounding tetragonal lattice, but $Mn^{4+}(t_{2g}{}^3, e_g{}^0)$ is not a JT ion. We can clearly observe in Figure 2 that the e_g orbital of Mn^{3+} atom in the

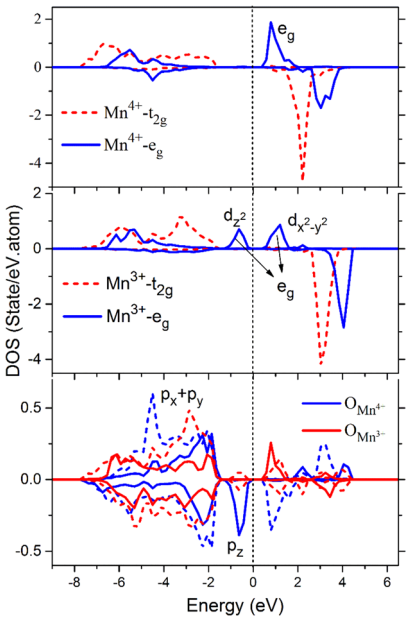

Figure 2. Projected density of states (DOS) of Mn-3d and O-2p. The solid and dashed lines in the upper panel represent Mn-e_g and Mn-t_{2g} orbitals, respectively. The O-p_z (solid lines) and O-$p_{x,y}$ orbitals (dashed lines) are shown in the lower panel. The zero of the energy is set to the Fermi level.

spin-up channel splits into a d_{z^2} orbital and $d_{x^2-y^2}$ orbital, opening a gap of about 0.5 eV between them.[18,19] The d_{z^2} orbital is filled while the $d_{x^2-y^2}$ orbital is unoccupied. This leads to a larger magnetic moment for Mn^{3+} compared with that of Mn^{4+}. By comparing the projected DOS of Mn and O, it is found that the Mn-d and O-p orbitals are hybridized to form covalent bonds between O and Mn. The profiles of p_x and p_y of O in both Mn^{3+} and Mn^{4+} layers are almost identical, and thus, the bond status of trivalent and quadrivalent Mn−O are basically the same in the (001) plane. An additional covalent

https://doi.org/10.1021/acsomega.1c01162
ACS Omega 2021, 6, 21255−21264

bond is formed just below the Fermi level by Mn^{3+}-d_{z^2} and O-p_z, which makes the structure more stable.

3.2. Isolated Point Defects. We then focus on single or isolated point defects in $LiMn_2O_4$. The following intrinsic defects are considered in this work: Li vacancy (V_{Li}), Mn vacancy (V_{Mn}), O vacancy (V_O), Li interstitial (I_{Li}), Mn interstitial (I_{Mn}), Li antisite (Li_{Mn}), and Mn antisite (Mn_{Li}).

The formation energy of a point defect E_f is defined as

$$E_f = E_{defect} - E_{bulk} - \sum_i n_i \mu_i \quad (1)$$

where E_{defect} and E_{bulk} are the total energies of the unit cell with and without the defect, respectively. The generation of defects involves adding atoms into or removing atoms from the unit cell. μ_i is the atomic chemical potential of species i, and n_i is the number of atoms i added to (positive) or removed from (negative) the lattice to produce the defect. The atomic chemical potential can also be written as $\mu_i = \mu_i^0 + \Delta\mu_i$, where μ_i^0 is the chemical potential of element i in its standard state. The standard states for Li and O are bcc Li and gaseous O_2, respectively. As for Mn, we choose the structure of $I\bar{4}3m$, which has different magnetic moments, as the standard state based on the previous theoretic and experimental works.[46]

The atomic chemical potentials are constrained by thermodynamic equilibrium conditions with various phases containing Li, Mn, and O. The existence of the $LiMn_2O_4$ phase requires a constraint on the chemical potentials as

$$\Delta\mu_{Li} + 2\Delta\mu_{Mn} + 4\Delta\mu_O = \Delta H_f(LiMn_2O_4) \quad (2)$$

where $\Delta H_f(LiMn_2O_4)$ is the enthalpy of formation of $LiMn_2O_4$. To calculate formation energies, one must obtain the values of $\Delta\mu_i$ (i = O, Li, and Mn). Another two linearly independent equations are needed in addition to eq 2. The synthesis processes of $LiMn_2O_4$ are usually in air;[10,47,48] thus, we assume O_2 is in equilibrium with the $LiMn_2O_4$ sample. In this case, the chemical potential of O is $\mu_o = \mu_o^0$, corresponding to the O-rich condition. The third constraint can be found from the observed phases in experiments. $LiMn_2O_4$ is synthesized by heating the mixing of Li salts and Mn-based oxides in air and the impurity phases Mn_2O_3, Mn_3O_4, $LiMnO_2$, and Li_2MnO_3 are generally present in the resulting samples.[47] Moreover, MnO_2 may also be present because it usually served as a reactant in some synthesis experiments.[10,48] So, the third limiting condition for chemical potentials can be derived from one of the five phases: monoclinic Li_2MnO_3 and $LiMnO_2$, cubic Mn_2O_3, tetragonal Mn_3O_4, and MnO_2. For instance, if $LiMn_2O_4$, O_2, and Mn_2O_3 are in equilibrium with each other, we get

$$2\Delta\mu_{Mn} + 3\Delta\mu_O = \Delta H_f(Mn_2O_3) \quad (3)$$

Here, $\Delta H_f(Mn_2O_3)$ is the enthalpy of formation of Mn_2O_3. The calculated formation enthalpies of $LiMn_2O_4$, Li_2MnO_3, $LiMnO_2$, Mn_2O_3, Mn_3O_4, and MnO_2 are shown in Table S1 and the atomic chemical potentials under various equilibrium conditions are in Table S2.

Table 1 lists defect formation energies at various O-rich equilibrium conditions. For vacancies, there are two kinds of Mn and O vacancies in $LiMn_2O_4$. We mark them as V_{Mn}^{III}, V_{Mn}^{IV}, V_O^{III}, and V_O^{IV} (superscripts III and IV indicate that atoms on the Mn^{3+} and the Mn^{4+} layers are removed to generate vacancies, respectively). For antisite defects, there is only one case of Mn antisite (a Mn locates in the Li site) and two types of Li antisites (a Li ion substitutes Mn^{3+} or Mn^{4+}, denoted as Li_{Mn}^{III} or Li_{Mn}^{IV}). The 16*c* Wyckoff site is the interstitial site for Li or Mn, which locates in the midpoint between two neighboring Li ions. The interstitials can occur in both the Mn^{3+} and the Mn^{4+} layers, and we also use III and IV to denote different interstitials of Li and Mn.

Table 1. Calculated Formation Energies E_f of Intrinsic Defects in $LiMn_2O_4$ under Some O-Rich Equilibrium Conditions[a]

	E_f (eV)				
defects	*a*	*b*	*c*	*d*	*e*
V_{Li}	1.22	0.46	0.38	−0.09	−0.22
V_{Mn}^{III}	0.22	0.60	0.64	0.88	0.94
V_{Mn}^{IV}	−0.13	0.25	0.29	0.53	0.59
V_O^{III}	2.28	2.28	2.28	2.28	2.28
V_O^{IV}	2.30	2.30	2.30	2.30	2.30
Li_{Mn}^{III}	−1.43	−0.29	−0.17	0.54	0.73
Li_{Mn}^{IV}	−1.22	−0.08	0.04	0.75	0.94
Mn_{Li}	2.84	1.70	1.58	0.87	0.68
I_{Li}^{III}	1.28	2.04	2.12	2.59	2.72
I_{Li}^{IV}	1.00	1.76	1.84	2.31	2.44
I_{Mn}^{III}	4.14	3.76	3.72	3.48	3.42
I_{Mn}^{IV}	3.98	3.60	3.56	3.32	3.26

[a] *a*, *b*, *c*, *d*, and *e* represent the $LiMnO_2$, Li_2MnO_3, MnO_2, Mn_2O_3, Mn_3O_4 phases that coexist with O_2 and $LiMn_2O_4$, respectively. The negative values of formation energies indicate that $LiMn_2O_4$ would spontaneously form defects, and therefore, the assumption of local equilibrium under those conditions indicates instability.

As we choose the O-rich condition, an environment that is more close to the experimental operation condition, to determine the chemical potentials for each of the elements, the formation energy of O vacancies is irrelevant to the equilibrium conditions. As shown in Table 2, the formation energies of V_O^{III} and V_O^{IV} are almost equal (2.28 and 2.30 eV), which are higher than that of other metal cation vacancies. Koyama et al. studied oxygen vacancy and metal interstitials in $LiMn_2O_4$ through the local spin density approximation (LSDA) and ultrasoft pseudopotentials based on FM configuration.[29] They reported that V_O has a formation energy of 2.17 eV when the chemical potential of oxygen is determined by the equilibrium between Mn_2O_3 and MnO_2. We also calculated the formation energy of V_O under the same conditions and found the value to be 1.81 eV. The difference may originate from the fact that we use different calculation methods and magnetic configurations of $LiMn_2O_4$ compared with Koyama's work.

The formation energy of V_{Li} is in the range of −0.22 to 1.22 eV, depending on the equilibrium conditions. It is found that the formation energy of V_{Li} is negative (−0.09 eV at condition *d* and −0.22 eV at condition *e*). A negative formation energy indicates that the system would spontaneously form defects, and therefore, the assumption of local equilibrium under those conditions indicates instability. Strictly speaking, the atomic chemical potentials are limited in a range that avoids the formation of competitive phases containing Li, O, and Mn. As for Mn vacancies, the formation energy of V_{Mn} is relatively low. The formation of V_{Mn}^{IV} is lower by 0.35 eV than that of V_{Mn}^{III}; thus, Mn vacancies are more likely to form in the Mn^{4+} layer. Note that the formation energy of V_{Mn}^{IV} is negative (−0.13 eV) at condition a, the environment that $LiMn_2O_4$, O_2, and $LiMnO_2$ are in equilibrium with each other. Again, this

https://doi.org/10.1021/acsomega.1c01162
ACS Omega 2021, 6, 21255−21264

Table 2. Distance $d_{X\text{-}O}$ between the Center of Defect X and Its Surrounding O Atoms[a]

	8*a*		16*d*		16*c*	
defects	V_{Li}	Mn_{Li}	Li_{Mn}^{III}	V_{Mn}^{IV}	I_{Mn}^{IV}	I_{Li}^{IV}
$d_{X\text{-}O}$ (Å)	2.00(×4)	2.04(×4)	2.17(×2)	2.33(×2)	1.96(×4)	1.93(×2)
			2.07(×4)	2.21(×4)	2.02(×2)	2.14(×2)
						2.40(×2)

[a]The values in parentheses indicate the number of X−O "bonds".

Table 3. Change in Bader Charges ΔQ of the Atoms Near Some Isolated Defects

		8*a*		16*d*		16*c*		32*e*
defects		V_{Li}	Mn_{Li}	Li_{Mn}	V_{Mn}	I_{Mn}	I_{Li}	V_O
ΔQ (e)	Mn			+0.13	+0.13	−0.13	−0.15	−0.20
	O	+0.14	−0.05	+0.05	+0.17	−0.02	−0.07	−0.02

indicates that the material would be unstable in the presence of O_2 and $LiMnO_2$.

The formation energies for vacancies are not very much high, and thus, they would appear in $LiMn_2O_4$ at a detectable concentration in the synthesis process. Tarascon et al. used the TGA measurement to test the effect of annealing temperatures on the oxygen content.[22] They found that at 1000°C, $LiMn_2O_4$ even has a reversible oxygen loss of 5% and forms $LiMn_2O_{3.8}$. Kanno et al. synthesized tetragonal spinel $LiMn_2O_4$ by quenching from 920°C, and the time-of-flight (TOF) neutron powder diffraction measurement shows that 3.5% O vacancies are generated and no significant stoichiometric composition deviation was observed at Li 8*a* and Mn 16d sites.[49]

As for cation antisites, namely, Li_{Mn}^{III}, Li_{Mn}^{IV}, and Mn_{Li}, we found that the formation energies of Li antisites were lower than that of the Mn antisite under most equilibrium conditions. The formation energy of Mn_{Li} is lower than that of Li antisites, just only under condition *e*. The calculated formation energies of these cation antisites do not exceed 3.0 eV and thus Mn_{Li} and Li_{Mn} are likely to appear in $LiMn_2O_4$, as revealed by several experiments.[22,33,47,50] Paulsen and Dahn have investigated in detail the phase diagram and the stability region of the Li−Mn−O spinel between 400 and 800 °C by various experimental methods[23]. They found that the thermodynamic stable phases in the range of 400−880 °C are only the spinel with the composition $Li_{1+x}Mn_{2-x}O_{4+\delta}$ ($\delta < 0.02$). If the temperature is above 800°C, the stable Li−Mn−O spinel is $Li_{1-x}Mn_{2+x}O_4$. In other words, Li_{Mn} and Mn_{Li} antisites generally appear in $LiMn_2O_4$ and make the spinel more stable.

Among interstitial defects, i.e., an external Li or Mn atom entering the empty 16*c* site, the formation energies of Li interstitials are moderate (1.0−2.44 eV for I_{Li}^{IV} and 1.28−2.72 eV for I_{Li}^{III}). Thus, the Li insertion process of $LiMn_2O_4$ is feasible and $LiMn_2O_4$ has the ability to accommodate extra Li ions. Moreover, the excess Li ions tend to occupy the 16*c* site of the Mn^{4+} layer. Yamada et al. found that excess Li would be preferably inserted into the interstitial 16*c* sites under reducing experimental conditions, forming tetragonal $Li_{1+x}Mn_2O_4$.[51] Gummow et al. also reported that tetragonal lithiated spinel $Li_2Mn_2O_4$ can be synthesized under appropriate reducing conditions.[52] As for Mn interstitial, the formation energy of it is so high that it is hard to form at the assumed equilibrium conditions.

The occurrence of defects can result in a local structural change. We show the distance between the defect X with the most stable configuration and its surrounding O atoms in Table 2. The bond length of O−Li in pristine $LiMn_2O_4$ is 2.00 Å. We found that V_{Li} had no significant influence on the original Li−O_4 tetrahedron, as the distance of V_{Li}−O is still 2.0 Å. When a Mn substitutes a Li to form Mn_{Li}, the length of Mn−O bonds in the Mn−O_4 tetrahedron is 2.04 Å, slightly larger than the bond length of O−Li. V_{Mn}^{IV} causes the original Mn−O_6 octahedron to expand. The distance of V_{Mn}^{IV}−O is 2.33 Å in the direction of *c*-axis and 2.21 Å in the *a*/*b* plane, while the bond lengths of Mn^{4+}−O are 1.96 and 1.93 Å in defect-free $LiMn_2O_4$. The outward relaxation of O is due to the missing of strong covalent bonds between O and Mn. Li_{Mn}^{III} mainly affects the O atoms in the Mn^{3+} plane. The four Mn^{3+}−O bonds in the (001) plane are 1.96−1.97 Å, but the distances of Li_{Mn}^{III}−O are elongated to 2.07 Å. For interstitial defects at the 16*c* site, the newly formed Mn−O_6 octahedron in the Mn^{4+} layer distorts slightly (two Mn−O bonds with a length of 2.02 Å and four Mn−O bonds with a length of 1.96 Å). In addition to O atoms being affected by the 16*c* Mn, we found that there was a repulsion for the adjacent 8*a* Li ions due to the Coulomb repulsive interaction between the interstitial Mn and Li cations, which increased the distance of 16*c* I_{Mn}^{IV} and 8*a* Li from 1.88 to 2.23 Å. I_{Li}^{IV} also affects its neighboring 8*a* Li, but the Coulomb repulsion effect is less compared with the case of Mn interstitial. The distance between Li (8a) and Li (16*c*) is 2.13 Å, which is 0.1 Å lower than the distance of Li (8a) and I_{Mn}^{IV}(16*c*). The occurrence of V_O^{III} causes the Li ion to directly deviate from the oxygen defect, resulting in a distance of V_O^{III}−Li to be 2.40 Å. Consequently, the other three Li−O bonds in the formed Li−O_3 unit due to the removal of a O atom are decreased to 1.89 Å.

3.3. Electronic Structure Analysis. When defects are generated in the lattice, atom's charge will rearrange, and charge compensation to the defects occurs. To understand the charge transfer between atoms when a defect exists, the Bader charges are calculated and shown in Table 3. If an exotic Mn is embedded into the 16*c* octahedral site, the interstitial Mn then bonds with its surrounding six oxygen atoms. The charge transfer in the lattice with an interstitial defect of I_{Mn} is mainly realized by changing the oxidation state of the lattice 16*d* Mn on the opposite side of the new bonding oxygen. That is to say, charge compensation in the case of Mn interstitial is carried out by the six Mn on the 180° I_{Mn}−O−Mn chain. By checking the Mn−O_6 octahedron in which the Bader charge of Mn decreased by 0.13 e, we found that it shows noticeable distortion. For the embedding of the low valence element of Li in the 16*c* site to form I_{Li}, the Bader charge of Mn in the direction of *b*-axis is decreased by 0.15 e. The V_O defect at the 32*e* site causes the reduction of the two Mn^{4+} bonded with the

https://doi.org/10.1021/acsomega.1c01162
ACS Omega 2021, 6, 21255−21264

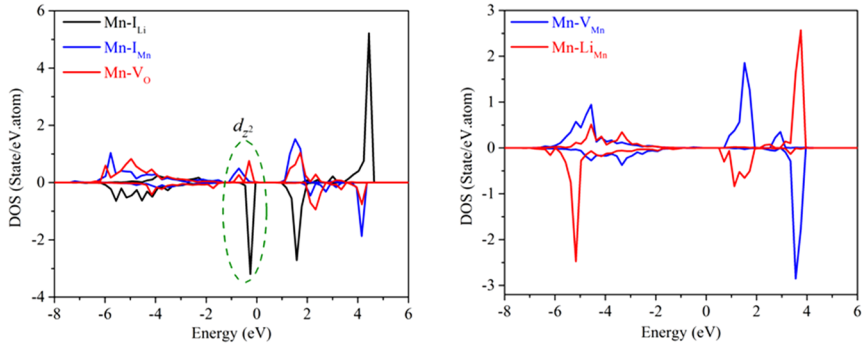

Figure 3. DOS of the e_g orbital of Mn around some point defects. The Fermi energy is set at zero.

Table 4. Binding Energy E_b between Some Isolated Point Defects

defect pair	$V_{Li}-V_{Li}$	$V_{Mn}^{III}-V_{Li}$	$V_O^{IV}-V_{Li}$	$Li_{Mn}^{III}-V_{Li}$	$I_{Mn}^{IV}-V_{Li}$	$I_{Mn}^{III}-V_{Mn}^{III}$
E_b (eV)	−0.05	0.18	−0.60	0.07	−1.76	−2.01
defect pair	$Mn_{Li}-V_{Li}$	$Mn_{Li}-Mn_{Li}$	$V_{Mn}^{III}-V_{Mn}^{IV}$	$Li_{Mn}^{III}-Li_{Mn}^{IV}$	$Li_{Mn}^{III}-Mn_{Li}$	$V_O^{III}-V_O^{III}$
E_b (eV)	−0.44	−0.47	1.93	0.85	−0.60	0.24

missing O to Mn^{3+} directly, as the Bader charge of the two Mn decreased by 0.20 e.

When a defect occurs in the 16*d* site (V_{Mn} and Li_{Mn}), it can be considered that the high-valence Mn is replaced by a low-valence element. At this time, the nearest Mn^{3+} (for Li_{Mn}^{III}, there are two Mn^{3+} and, for V_{Mn}^{IV}, there are four Mn^{3+}) is oxidized to Mn^{4+} for charge compensation, as its Bader charge is increased by 0.13 e in the two cases. Thus, V_{Mn} or Li_{Mn} gives rise to an increase in Mn^{4+} ions and subsequently a decrease in Mn^{3+} ions. As a result, the JT distortion around the defects is suppressed and the stability of the spinel structure is increased. The powder neutron-diffraction study, which did not detect any structural phase transition from 4 to 290 K, verified the stability of Li-substituted spinel $LiMn_{1.96}Li_{0.04}O_4$.[53]

However, if the defect is in the 8*a* site (V_{Li} and Mn_{Li}), it affects the Bader charge of the O in the $X-O_4$ tetrahedron directly (again, here, X represents the defect) and has no obvious effects on the charge of the surrounding Mn ions. Especially for V_{Li}, the charge of the surrounding O decreased by 0.14 e.

The charge transfer in the defective lattice is further illustrated by the DOS of the e_g state of Mn. As can be seen from Figure 3, in the case of I_{Li}, I_{Mn}, and V_O, the original Mn^{4+} around defects is reduced to Mn^{3+}, which is manifested by the split of the e_g orbital and the formation of a low-energy d_{z^2} orbital below the Fermi level. For the defects of V_{Mn} and Li_{Mn}, charge compensation is carried out by the surrounding Mn^{3+} oxidation to Mn^{4+}. These two kinds of defects can reduce the JT distortion around the defects, and the original d_{z^2} orbital also disappears.

3.4. Defect pairs. The electrostatic and elastic interactions between point defects may cause the clustering or association of some defects. Thus, in this section, we investigate the interactions between some point defects.

The binding energy E_b between isolated defects A and B is defined as follows

$$E_b = E_f(AB) - E_f(A) - E_f(B) \quad (4)$$

$E_f(AB)$ is the formation energy when defects A and B exist in the nearest-neighbor mode, and $E_f(A)$ and $E_f(B)$ are the formation energies of isolated defects A and B, respectively. The above definition shows that if the binding energy is negative, defects A and B have an attractive interaction; otherwise, defects A and B show a repulsive interaction. We choose the lowest energy configuration of the defect pair to calculate the formation energies of defect pairs and the corresponding binding energies between point defects.

The formation energies of some defect pairs under our considered thermodynamic equilibrium conditions are shown in Table S3. It is found that the formation energies of defect pairs $V_{Li}-V_{Li}$, $V_{Mn}^{III}-V_{Li}$, $Mn_{Li}-V_{Li}$, $Li_{Mn}^{III}-V_{Li}$, $Li_{Mn}^{III}-Li_{Mn}^{IV}$, $Mn_{Li}-Mn_{Li}$ and $Mn_{Li}-Li_{Mn}^{III}$ are less than 1.0 eV under some equilibrium conditions; thus, these defect pairs may occur in $LiMn_2O_4$ with detectable concentrations in the experimental synthesis process. Defect pairs $I_{Mn}^{IV}-V_{Li}$ and $V_O^{IV}-V_{Li}$ in some cases have moderate formation energy (1.0 − 1.6 eV), indicating the two defect pairs may also appear in the $LiMn_2O_4$. However, the pairs of Mn vacancy, O vacancy, and $I_{Mn}^{III}-V_{Mn}^{III}$ are hard to form due to their high formation energy, especially for O vacancy. Among these defect pairs, we pay particular attention to the cation exchange defect, i.e., the $Mn_{Li}-Li_{Mn}^{III}$ defect pair because cation mixing is common in cathode materials.[39,54,55] The formation energy of $Mn_{Li}-Li_{Mn}^{III}$ is 0.81 eV. Therefore, a considerable concentration of Li/Mn exchange defect can be observed in $LiMn_2O_4$ samples prepared by various experimental methods. By using the X-ray diffraction technique, Tarascon et al. reported that the amount of Li/Mn mixing can reach 10% in $LiMn_2O_4$ powders.[22]

Then, we consider the binding energy between point defects. The binding energy is independent of the atomic chemical potentials and is listed in Table 4.

We observe that the interaction between V_{Li} is rather weak, as the binding energy between V_{Li} is −0.05 eV. This finding is consistent with the nature of the ionic bond for Li, and thus, Li vacancies are prone to distribute in the lattice randomly. The pair $Li_{Mn}^{III}-V_{Li}$ also shows a small binding energy (0.07 eV), so the Li antisite has a weak repulsive interaction with Li vacancy. $I_{Mn}^{IV}-V_{Li}$, $V_O^{IV}-V_{Li}$,$Mn_{Li}-V_{Li}$, $Mn_{Li}-Mn_{Li}$, $I_{Mn}^{III}-V_{Mn}^{III}$, and $Li_{Mn}^{III}-Mn_{Li}$ have obviously negative binding energies, indicating that the defect pairs are more stable than the corresponding isolated defects. The exchange defect of $Mn_{Li}-Li_{Mn}$ has a large attractive effect. The binding energy between Mn_{Li} and Li_{Mn}^{III} is −0.60 eV, and thus the two types of defects tend to cluster. The clustering of cation exchange defects is also found in other

https://doi.org/10.1021/acsomega.1c01162
ACS Omega 2021, 6, 21255−21264

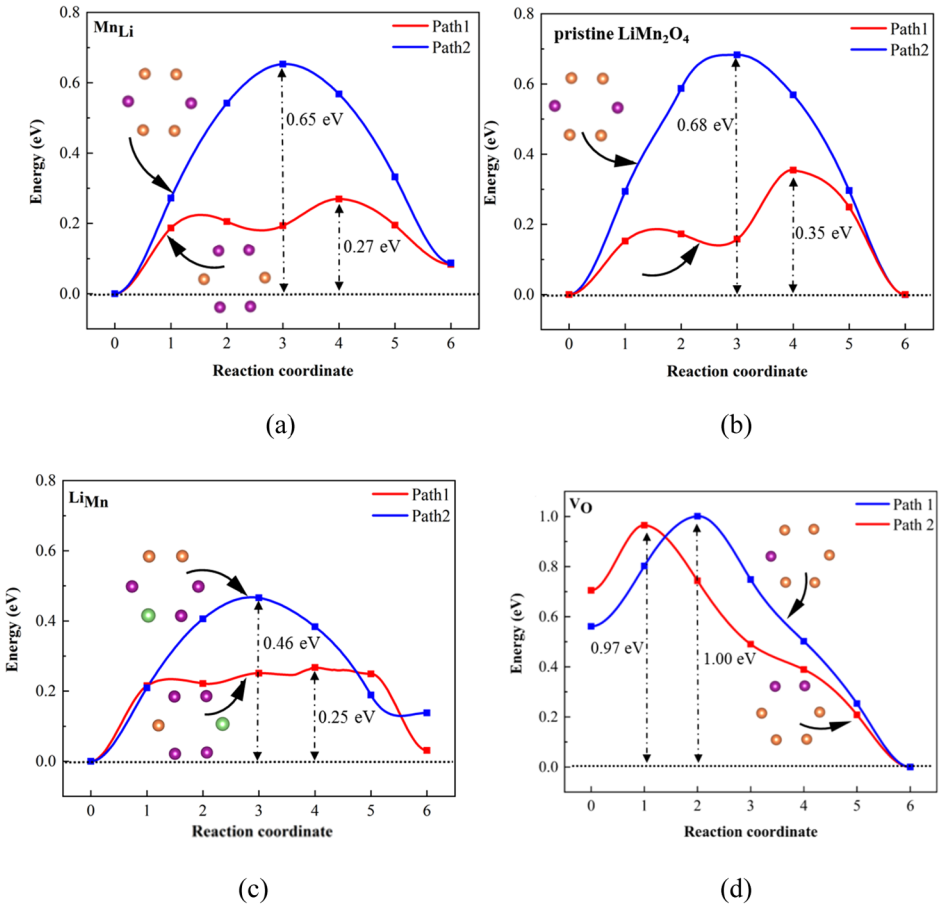

Figure 4. Calculated diffusion barriers of Li along different paths. (a) Li diffusion in pristine $LiMn_2O_4$; (b) Li diffusion in $LiMn_2O_4$ with a Mn_{Li} defect; (c) Li diffusion in $LiMn_2O_4$ with a Li_{Mn} defect; and (d) Li diffusion in $LiMn_2O_4$ with V_O. The inset shows the six-membered ring in the diffusion paths. Orange, purple, and green balls represent Mn^{3+}, Mn^{4+}, and Li, respectively.

cathode materials, such as in $LiFePO_4$.[56] I_{Mn} and V_{Li} have an extremely high binding energy (−1.76 eV), showing a strong agglomeration phenomenon. So, Li vacancies are prone to be formed near the Mn interstitial. O vacancies tend to be separated, as the binding energy between them is positive (0.24 eV). The binding energy of the Li_{Mn} antisite is 0.85 eV, hinting that Li_{Mn} would not be clustering. There is a strong repulsion between V^{III}_{Mn}−V^{IV}_{Mn}, as the binding energy between V^{III}_{Mn} and $V^{IV,}_{Mn}$ is a significant positive value (1.93 eV). The result is in accordance with the finding that V^{III}_{Mn}−V^{IV}_{Mn} has relatively high formation energy.

The Frenkel defect can be regarded as a kind of defect pair, namely an interstitial in 16*c* site plus a vacancy near it. Our calculated results show that the Li-Frenkel is unstable. After the structural relaxation for the Li-Frenkel, it was found that the Li atom at the 16*c* site moves back to its original 8*a* site, forming the pristine lattice again. This suggests that the generation of Li-Frenkel in $LiMn_2O_4$ is impossible. For the Mn-Frenkel defect, i.e., the defect pair I_{Mn}−V_{Mn}, the lowest energy configuration is I^{III}_{Mn}−V^{III}_{Mn} with a binding energy of −2.01 eV, showing significant attraction between I_{Mn} and V_{Mn}. So, the 16*c* Mn atom tends to approach the lattice 16*d* site if there is a Mn vacancy around it.

Huang et al. investigated the local structure of Li and O in oxygen-deficient tetragonal $LiMn_2O_4$ with a spherical aberration-corrected scanning transmission electron microscope (STEM) and first-principles calculations.[33] They revealed that Li ions move away from their ideal positions due to the presence of oxygen vacancies, resulting in defect complexes formed by Li and O vacancies. Their finding is consistent with our result that V^{IV}_O and V_{Li} have a strong attractive interaction. Koyama et al. studied O vacancy and interstitials of Li and Mn in the cubic $LiMn_2O_4$ by first-principles calculations based on FM configuration.[29] They revealed that when a Mn interstitial is placed at the 16*c* site, the configuration that a Li atom near the interstitial moves into the other neighboring 16*c* site has low energy compared with the simple interstitial lattice structure. That is, Li vacancy is prone to form near the interstitial Mn. The present finding that I^{IV}_{Mn} and V_{Li} have a strong attractive interaction is qualitatively in accordance with the conclusion of Koyama et al.

3.5. Diffusion of Li in $LiMn_2O_4$. Diffusion of Li is an important elementary step in the charge/discharge process in electrode materials. As for $LiMn_2O_4$, the diffusion of Li is mediated via the vacancy mechanism, which is composed of a series of jumps of Li ions between two 8*a* sites through a 16*c* site. In this section, we discuss the effect of point defects on the migration of Li ions.

After a Li vacancy is generated, the neighboring Li atom is allowed to migrate to the vacancy site through a 'ring' consisting of six Mn^{3+}/Mn^{4+} ions, that is, the Li ion jumps over the 16*c* octahedron sharing edges with six Mn−O_6 octahedrons. Usually, there are two kinds of Mn6 rings, as depicted in Figure 1b. We named the diffusion path that composes of four Mn^{4+} and two Mn^{3+} in the Mn6 ring as Path 1. The center of the 16*c* site in Path 1 is located on the Mn^{3+}

https://doi.org/10.1021/acsomega.1c01162
ACS Omega 2021, 6, 21255−21264

layer. The path involves migration across the Mn6 ring composed of two Mn^{4+} and four Mn^{3+} is named Path 2 in which the 16*c* site is located on the Mn^{4+} layer. We use the CINEB method with five images to study the diffusion behavior of Li going through the two different diffusion paths. We first investigate the diffusion of Li in pristine $LiMn_2O_4$. The calculated migration barrier of Li is shown in Figure 4a. Due to the different oxidation states of Mn in Path 1 and Path 2, the volume of the 16*c* octahedron and the electrostatic interaction between Mn and the migrated Li are different. We clearly observe different Li diffusion barriers for the two paths (0.35 eV for Path 1 and 0.68 eV for Path 2). Our calculated diffusion barriers are generally in agreement with the previous theoretic values based on the same magnetic configuration.[21,30] Xiao et al. reported that the migration barrier is 0.38 eV for Path 1,[30] and a barrier of 0.23 eV for Path 1 and 0.70 eV for Path 2 were reported by Liu et al.[21] We also found that a metastable configuration is reached when Li diffuses via Path 2. This configuration corresponds to the migrated Li at the 16*c* position in the center of the Mn6 ring. By comparison of the two paths, it is obvious that Li ions can easily diffuse through the path with more Mn^{4+} ions. The reason for the lower migration barrier of Li in Path 2 can be attributed to the electrostatic interaction between cations. Compared with Mn^{3+}, Mn^{4+} has a smaller electron cloud range, and thus, Mn^{4+} ions have a small Coulomb repelling effect on the mobile Li ions. Thus, if the symmetry is consistent, the higher the Mn^{4+} ratio, the lower the migration barrier of Li. We further speculate that a higher oxidized ion substituting a Mn in the Mn6 ring would increase the Li diffusion kinetics in spinel $LiMn_2O_4$.

Then, we consider the effects of point defects on the migration of Li. For this purpose, the defects with the lowest energy in each type are only considered, and Li vacancy is generated in the neighboring of the defect to study the migration process. The interstitials are not considered because they are located in the 16*c* site and hence block the diffusion of Li. The defects considered here are Mn_{Li}, Li^{III}_{Mn}, and V_O, which are commonly observed in experiments.

The calculated energy barriers of Li migration in the lattice with defects of Mn_{Li}, Li_{Mn}, and V_O are shown in Figure 4b,c,d, respectively. One should note that in some cases the Mn6 ring in the diffusion path is different from that of pristine $LiMn_2O_4$ because of charge transfer. The six-membered rings in the migration paths of the defective cell are also shown in the inset of Figure 4b,c,d. Mn_{Li} is the defect that a Mn is in a Li site (8*a* site), which does not change the oxidation state of Mn of the diffusion ring. The diffusion energy barriers for Li migrating through Paths 1 and 2 are 0.27 and 0.65 eV, respectively. Compared with Li diffusion in defect-free $LiMn_2O_4$, it is revealed that Mn_{Li} leads to a decrease in the diffusion barrier of Li slightly. As for the antisite Li_{Mn}, Li is prone to substitute Mn^{3+}. In this case, the Mn6 ring in the diffusion channel is changed to a Mn5Li ring, that is to say, the ring is composed of five Mn ions and one Li ion. The diffusion barriers of Path 1 and Path 2 are 0.25 and 0.46 eV, respectively. The diffusion barrier of Li is reduced by 0.1 or 0.22 eV in comparison with that of Li diffusion in perfect $LiMn_2O_4$. This is because the Coulomb repulsive interaction of Li−Li is much weaker than that of Li−Mn^{3+}. Xiao et al. have studied Li diffusion in Li-excess $LiMn_2O_4$ by first-principles calculations.[30] They found that when a Mn^{3+} in the Mn6 ring is replaced by a Li, the diffusion barrier of Li is 0.24 or 0.29 eV, depending on the atomic arrangement of Mn^{4+}, Mn^{3+}, and Li^+ in the ring. The presently calculated diffusion barrier of Path 1 is in good agreement with their result.

When an anion defect (i.e., O vacancy) is present in the lattice, Li ions around it have a strong tendency to move outward from the V_O defect, and the previous study has shown that two Mn^{4+} around it are reduced to Mn^{3+}. In this case, the Mn6 ring in the diffusion path is also different from the Mn6 ring of the perfect lattice, as shown in Figure 4d. The energy barriers for Li migrating through Path 1 (0.97 eV) and Path 2 (1.0 eV) are almost equal. The higher diffusion barrier in the case of V_O is mainly caused by the charge distribution of the Mn ring in the diffusion path. Both Path 1 and Path 2 in the case of V_O are asymmetrically arranged in the Mn ring and have a high ratio of Mn^{3+} ions, and this causes much more serious JT distortion and coulombic repulsion between Mn and migrated Li.

By studying the influence of point defects on the diffusion energy barrier of Li, we found that both Li_{Mn} and Mn_{Li} antisites can effectively reduce the diffusion energy barrier, but V_O results in an increase of diffusion barrier significantly. One should be aware that the kinetics process for Li migration is not only determined by the migration barrier but also by the concentration of point defects in the lattice. Consequently, if the antisite defects or the cation mixing is at a high concentration, they could promote Li diffusion kinetics. From an experimental point of view, 10% cation mixing could be achieved by adjusting the synthesis conditions.[22] Such defect concentration is relatively considerable and it is possible to measure the diffusion kinetics of Li ions in $LiMn_2O_4$ samples with cation mixing. Hence, cation mixing is beneficial for improving the charge/discharge rate of $LiMn_2O_4$.

4. CONCLUSIONS

In summary, defect properties of spinel $LiMn_2O_4$ were studied by means of first-principles calculations based on a reasonable magnetic configuration. The formation energies of intrinsic defects of vacancies, interstitials, and cation antisites were calculated under assumed equilibrium conditions and the binding energies of some defect pairs were calculated to determine the clustering of some point defects. Charge distribution and compensation involving the creation of defects were also investigated. The present work reveals that O, Mn, and Li vacancies, Mn and Li antisites, and Li interstitial may exist in $LiMn_2O_4$, but their concentrations are sensitive to experimental conditions and thermal history. The defect pairs $I^{IV}_{Mn}-V_{Li}$, $V^{IV}_O-V_{Li}$, $Mn_{Li}-V_{Li}$, $Mn_{Li}-Mn_{Li}$, $I^{II}_{Mn}I-V^{III}_{Mn}$, and $Li^{III}_{Mn}-Mn_{Li}$ are more stable than corresponding isolated defects. The charge compensation associated with the creation of defects was also determined according to Bader charges. We found that the compensation was mainly achieved through the redox of the surrounding Mn^{3+}/Mn^{4+}, except for the case of defects at the 8*a* site. Finally, the diffusion of Li ions around defects was studied. It was found that O vacancy significantly increased the diffusion barrier of Li. In contrast, the antisite defects, i.e., Li_{Mn} and Mn_{Li}, decreased the Li diffusion barrier obviously. Our theoretical studies provide clear information on the defect properties in $LiMn_2O_4$ on the atomic scale and could help in adjusting the performance of spinel $LiMn_2O_4$ from defect engineering.

https://doi.org/10.1021/acsomega.1c01162
ACS Omega 2021, 6, 21255−21264

■ ASSOCIATED CONTENT

Supporting Information

The Supporting Information is available free of charge at https://pubs.acs.org/doi/10.1021/acsomega.1c01162.

The calculated formation enthalpies of $LiMn_2O_4$, Li_2MnO_3, $LiMnO_2$, Mn_2O_3, MnO_2, and Mn_3O_4 (Table S1); the calculated chemical potentials of Li and Mn at some equilibrium conditions (Table S2); and the calculated formation energies of defect pairs with the lowest energy configuration (Table S3) (PDF)

■ AUTHOR INFORMATION

Corresponding Author

Jianchuan Wang − *State Key Laboratory of Powder Metallurgy, Central South University, Changsha 410083, China*; orcid.org/0000-0001-7265-5186; Email: jcw728@126.com

Authors

Xu Li − *State Key Laboratory of Powder Metallurgy, Central South University, Changsha 410083, China*

Shiwei Zhang − *State Key Laboratory of Powder Metallurgy, Central South University, Changsha 410083, China*

Lixian Sun − *Guangxi Key Laboratory of Information Materials, Guilin University of Electronic Technology, Guilin 541004, China*

Weibin Zhang − *Key Laboratory for Liquid-Solid Structural Evolution and Processing of Materials (Ministry of Education), Shandong University, Jinan 250061, China*; orcid.org/0000-0001-6584-5053

Feng Dang − *Key Laboratory for Liquid-Solid Structural Evolution and Processing of Materials (Ministry of Education), Shandong University, Jinan 250061, China*

Hans J. Seifert − *Institute for Applied Materials—Applied Materials Physics, Karlsruhe Institute of Technology, Karlsruhe 76344, Germany*

Yong Du − *State Key Laboratory of Powder Metallurgy, Central South University, Changsha 410083, China*

Complete contact information is available at: https://pubs.acs.org/10.1021/acsomega.1c01162

Notes

The authors declare no competing financial interest.

■ ACKNOWLEDGMENTS

This work was funded by the Sino-German Center for Promotion of Science (Grant No. GZ 1528) and Guangxi Key Laboratory of Information Materials (201013-K).

■ REFERENCES

(1) Bäuerlein, P.; Herr, R.; Kloss, M.; Kümpers, J.; Maul, M.; Meissner, E. Advanced lithium ion cells with lithium manganese spinel. *J. Power Sources* **1999**, *81*−*82*, 585−588.

(2) Gummow, R. J.; Kock, A. D.; Thackeray, M. M. Improved capacity retention in rechargeable 4 V lithium/lithium-manganese oxide (spinel) cells. *Solid State Ionics* **1994**, *69*, 59−67.

(3) Guyomard, D.; Tarascon, J. M. The carbon/$Li_{1+x}Mn_2O_4$ system. *Solid State Ionics* **1994**, *69*, 222−237.

(4) Thackeray, M.; David, W.; Bruce, P.; Goodenough, J. B. Lithium insertion into manganese spinels. *Mater. Res. Bull.* **1983**, *18*, 461−472.

(5) Manev, V.; Banov, B.; Momchilov, A.; Nassalevska, A. $LiMn_2O_4$ for 4 V lithium-ion batteries. *J. Power Sources* **1995**, *57*, 99−103.

(6) Prabaharan, S.; Saparil, N. B.; Michael, S.; Massot, M.; Julien, C. Soft-chemistry synthesis of electrochemically-active spinel $LiMn_2O_4$ for Li-ion batteries. *Solid State Ionics* **1998**, *112*, 25−34.

(7) Son, J.; Kim, H. G.; Park, Y. New preparation method and electrochemical property of $LiMn_2O_4$ electrode. *Electrochim. Acta* **2004**, *50*, 453−459.

(8) Zhang, S.; Jow, T. Optimization of synthesis condition and electrode fabrication for spinel $LiMn_2O_4$ cathode. *J. Power Sources* **2002**, *109*, 172−177.

(9) Takada, T.; Hayakawa, H.; Enoki, H.; Akiba, E.; Slegr, H.; Davidson, I.; Murray, J. Structure and electrochemical characterization of $Li_{1+x}Mn_{2-x}O_4$ spinels for rechargeable lithium batteries. *J. Power Sources* **1999**, *81*−*82*, 505−509.

(10) Rouse, G.; Masquelier, C.; Rodriguez-Carvajal, J.; Hervieu, M. Cubic Orthorhombic Transition in the Stoichiometric Spinel $LiMn_2O_4$. *Electrochem. Solid-State Lett.* **1999**, *2*, 6−8.

(11) Ram, P.; Gören, A.; Carlos, M.; Ferdov, S.; Silva, M. M.; Singhal, R.; Costa, C. M.; Lanceros-Mendez, S. Improved performance of rare earth doped $LiMn_2O_4$ cathodes for lithium-ion battery applications. *New J. Chem.* **2016**, *40*, 6244−6252.

(12) Liu, T.; Dai, A.; Lu, J.; et al. Correlation between manganese dissolution and dynamic phase stability in spinel-based lithium-ion battery. *Nat. Commun.* **2019**, *10*, No. 4721.

(13) Lei, S. M. Small polaron migration in $Li_xMn_2O_4$: From first principles calculations. *Phys. Lett. A* **2009**, *373*, 2796−2799.

(14) Karim, A.; Fosse, S.; Persson, K. A. Surface structure and equilibrium particle shape of the $LiMn_2O_4$ spinel from first-principles calculations. *Phys. Rev. B* **2013**, *87*, No. 075322.

(15) Nakayama, M.; Nogami, M. A first-principles study on phase transition induced by charge ordering of Mn^{3+}/Mn^{4+} in spinel $LiMn_2O_4$. *Solid State Commun.* **2010**, *150*, 1329−1333.

(16) Rodríguez-Carvajal, J.; Rousse, G.; Masquelier, C.; Hervieu, M. Electronic crystallization in a lithium battery material: columnar ordering of electrons and holes in the spinel $LiMn_2O_4$. *Phys. Rev. Lett.* **1998**, *81*, 4660−4663.

(17) Singh, G.; Gupta, S. L.; Prasad, R.; Auluck, S.; Gupta, R.; Sil, A. Suppression of Jahn-Teller distortion by chromium and magnesium doping in spinel $LiMn_2O_4$: A first-principles study using GGA and GGA+*U*. *J. Phys. Chem. Solids* **2009**, *70*, 1200−1206.

(18) Ouyang, C. Y.; Shi, S. Q.; Lei, M. S. Jahn−Teller distortion and electronic structure of $LiMn_2O_4$. *J. Alloys Compd.* **2009**, *474*, 370−374.

(19) Lee, Y. K.; Park, J.; Lu, W. Electronic and Bonding Properties of $LiMn_2O_4$ Spinel with Different Surface Orientations and Doping Elements and Their Effects on Manganese Dissolution. *J. Electrochem. Soc.* **2016**, *163*, A1359−A1368.

(20) Hoang, K. Understanding the electronic and ionic conduction and lithium over-stoichiometry in $LiMn_2O_4$ spinel. *J. Mater. Chem. A* **2014**, *2*, 18271−18280.

(21) Liu, W. W.; Wang, D.; Wang, Z.; Deng, J.; Zhang, Y.; Lau, W.-M. Influence of magnetic ordering and Jahn−Teller distortion on the lithiation process of $LiMn_2O_4$. *Phys. Chem. Chem. Phys.* **2017**, *19*, 6481−6486.

(22) Tarascon, J.; McKinnon, W.; Coowar, F.; Bowmer, T.; Amatucci, G.; Guyomard, D. Synthesis conditions and oxygen stoichiometry effects on Li insertion into the spinel $LiMn_2O_4$. *J. Electrochem. Soc.* **1994**, *141*, 1421−1431.

(23) Paulsen, J.; Dahn, J. Phase diagram of Li−Mn−O spinel in air. *Chem. Mater* **1999**, *11*, 3065−3079.

(24) Dong, H. J.; Shin, Y. J.; Oh, S. M. Dissolution of Spinel Oxides and Capacity Losses in 4 V $Li/Li_xMn_2O_4$ Cells. *J. Electrochem. Soc.* **1996**, *143*, 2204−2211.

(25) Sugiyama, J.; Atsumi, T.; Hioki, T.; Noda, S.; Kamegashira, N. Nonstoichiometry and defect structure of spinel $LiMn_2O_{4-\delta}$. *J. Power Sources* **1997**, *68*, 641−645.

(26) Xia, Y.; Sakai, T.; Fujieda, T.; Yang, X. Q.; Sun, X.; Ma, Z. F.; Mcbreen, J.; Yoshio, M. Correlating Capacity Fading and Structural Changes in $Li_{1+y}Mn_{2-y}O_{4-\delta}$ Spinel Cathode Materials: A Systematic

Study on the Effects of Li/Mn Ratio and Oxygen Deficiency. *J. Electrochem. Soc.* **2001**, *148*, A723−A729.
(27) Wang, J.; Du, Y.; Xu, H.; Jiang, C.; Kong, Y.; Sun, L.; Liu, Z.-K. Native defects in $LiNH_2$: A first-principles study. *Phys. Rev. B* **2011**, *84*, No. 024107.
(28) Wang, J.; Du, Y.; Sun, L. Understanding of hydrogen desorption mechanism from defect point of view. *Natl. Sci. Rev.* **2018**, *5*, 318−320.
(29) Koyama, Y.; Tanaka, I.; Adachi, H.; Uchimoto, Y.; Wakihara, M. First principles calculations of formation energies and electronic structures of defects in oxygen-deficient $LiMn_2O_4$. *J. Electrochem. Soc.* **2003**, *150*, A63−A67.
(30) Xiao, W.; Xin, C.; Li, S.; Jie, J.; Gu, Y.; Zheng, J.; Pan, F. Insight into fast Li diffusion in Li-excess spinel lithium manganese oxide. *J. Mater. Chem. A* **2018**, *6*, 9893−9898.
(31) Xu, B.; Meng, S. Factors affecting Li mobility in spinel $LiMn_2O_4$- A first-principles study by GGA and GGA+*U* methods. *J. Power Sources* **2010**, *195*, 4971−4976.
(32) Ammundsen, B.; Rozière, J.; Islam, M. S. Atomistic Simulation Studies of Lithium and Proton Insertion in Spinel Lithium Manganates. *J. Phys. Chem. B* **1997**, *101*, 8156−8163.
(33) Huang, R.; Ikuhara, Y. H.; Mizoguchi, T.; Findlay, S. D.; Kuwabara, A.; Fisher, C. A. J.; Moriwake, H.; Oki, H.; Hirayama, T.; Ikuhara, Y. Oxygen-vacancy ordering at surfaces of lithium manganese(III,IV) oxide spinel nanoparticles. *Angew. Chem.* **2011**, *123*, 3109−3113.
(34) Kresse, G. G.; Furthmüller, J. J. Efficient Iterative Schemes for Ab Initio Total-Energy Calculations Using a Plane-Wave Basis Set. *Phys. Rev. B* **1996**, *54*, No. 11169.
(35) Perdew, J. P.; Burke, K.; Ernzerhof, M. Generalized Gradient Approximation Made Simple. *Phys. Rev. Lett.* **1996**, *77*, 3865−3868.
(36) Perdew, J. P.; Yue, W. Accurate and Simple Analytic Representation of the Electron-Gas Correlation Energy. *Phys. Rev. B* **1992**, *45*, 13244−13249.
(37) Wang, Y.; Perdew, J. P. Correlation hole of the spin-polarized electron gas, with exact small-wave-vector and high-density scaling. *Phys. Rev. B* **1991**, *44*, 13298−13307.
(38) Anisimov, V. I.; Zaanen, J.; Andersen, O. K. Band Theory and Mott Insulators: Hubbard U Instead of Stoner I. *Phys. Rev. B* **1991**, *44*, 943−954.
(39) Shiiba, H.; Zettsu, N.; Nakayama, M.; Oishi, S.; Teshima, K. Defect formation energy in spinel $LiNi_{0.5}Mn_{1.5}O_{4-\delta}$ using Ab initio DFT calculations. *J. Phys. Chem. C* **2015**, *119*, 9117−9124.
(40) Kitchaev, D.; Peng, H.; Liu, Y.; Sun, J.; Perdew, J. P.; Ceder, G. Energetics of MnO_2 polymorphs in density functional theory. *Phys. Rev. B* **2016**, *94*, No. 045132.
(41) Henkelman, G.; Jónsson, H. Improved tangent estimate in the nudged elastic band method for finding minimum energy paths and saddle points. *J. Chem. Phys.* **2000**, *113*, 9978−9985.
(42) Henkelman, G.; Uberuaga, B. P.; Jónsson, H. A climbing image nudged elastic band method for finding saddle points and minimum energy paths. *J. Chem. Phys.* **2000**, *113*, 9901−9904.
(43) Tang, W.; Sanville, E.; Henkelman, G. A grid-based Bader analysis algorithm without lattice bias. *J. Phys.: Condens. Matter* **2009**, *21*, No. 084204.
(44) Sanville, E.; Kenny, S. D.; Smith, R.; Henkelman, G. Improved grid-based algorithm for Bader charge allocation. *J. Comput. Chem.* **2007**, *28*, 899−908.
(45) Yamaguchi, H.; Yamada, A.; Uwe, H. Jahn-Teller transition of $LiMn_2O_4$ studied by x-ray-absorption spectroscopy. *Phys. Rev. B* **1998**, *58*, 8−11.
(46) Sliwko, V.; Mohn, P.; Schwarz, K. The electronic and magnetic structures of alpha - and beta -manganese. *J. Phys: Condens. Matter* **1994**, *6*, 6557−6564.
(47) Tarascon, J.; Coowar, F.; Amatuci, G.; Shokoohi, F.; Guyomard, D. The $Li_{1+x}Mn_2O_4C$ system Materials and electrochemical aspects. *J. Power Sources* **1995**, *54*, 103−108.
(48) Strobel, P.; Rousse, G.; Ibarra-Palos, A.; Masquelier, C. Disproportionation of stoichiometric $LiMn_2O_4$ on annealing in oxygen. *J. Solid State Chem.* **2004**, *177*, 1−5.
(49) Kanno, R.; Kondo, A.; Yonemura, M.; Gover, R.; Kawamoto, Y.; et al. The relationships between phases and structures of lithium manganese spinels. *J. Power Sources* **1999**, *81*−*82*, 542−546.
(50) Gao, Y.; Dahn, J. R. Thermogravimetric analysis to determine the lithium to manganese atomic ratio in $Li_{1+x}Mn_{2-x}O_4$. *Appl. Phys. Lett.* **1995**, *66*, 2487−2489.
(51) Yamada, A. Lattice instability in Li $(Li_xMn_{2-x})O_4$. *J. Solid State Chem.* **1996**, *122*, 160−165.
(52) Gummow, R. J.; Thackeray, M. M. An Investigation of Spinel-Related and Orthorhombic $LiMnO_2$ Cathodes for Rechargeable Lithium Batteries. *J. Electrochem. Soc.* **1994**, *141*, 1178−1182.
(53) Verhoeven, V. W. J.; Mulder, F. M.; Schepper, I. M. d. Influence of Mn by Li substitution on the Jahn−Teller distortion in $LiMn_2O_4$. *Phys. B* **2000**, *276*−*278*, 950−951.
(54) Seo, D.-H.; Lee, J.; Urban, A.; Malik, R.; Kang, S.; Ceder, G. The structural and chemical origin of the oxygen redox activity in layered and cation-disordered Li-excess cathode materials. *Nat. chem.* **2016**, *8*, 692−697.
(55) Chen, J.; Graetz, J. Study of antisite defects in hydrothermally prepared $LiFePO_4$ by in situ X-ray diffraction. *ACS Appl. Mater. Interfaces* **2011**, *3*, 1380−1384.
(56) Chung, S. Y.; Choi, S. Y.; Yamamoto, T.; Ikuhara, Y. Atomic-scale visualization of antisite defects in $LiFePO_4$. *Phys. Rev. Lett.* **2008**, *100*, No. 125502.

https://doi.org/10.1021/acsomega.1c01162
ACS Omega 2021, 6, 21255−21264